photonics

MDPI

Article

Reliability Prediction of TFT-LCD Modules in Harsh Environments Using Physics-Guided Machine Learning

Rui Zhou [1], Han Li [2], Xiaoqin Wei [2,*], Haitao Zhu [3], Xu Zhou [3], Xiaojie Li [3], Rihui Yao [1,3], Wei Xu [1,3], Honglong Ning [1,3,*] and Junbiao Peng [1]

[1] State Key Laboratory of Luminescent Materials and Devices, Guangdong Basic Research Center of Excellence for Energy & Information Polymer Materials, School of Materials Sciences and Engineering, South China University of Technology, Guangzhou 510640, China
[2] Southwest Institute of Technology and Engineering, Chongqing 400039, China
[3] Shenzhen Yaham Optoelectronics., Co., Ltd., Shenzhen 518103, China
* Correspondence: weixiaoqin810913@163.com (X.W.); ninghl@scut.edu.cn (H.N.)

Abstract

Accurate Remaining Useful Life (RUL) prediction of TFT-LCD modules is critical for industrial predictive maintenance, yet it remains heavily challenged by complex degradation mechanisms in different climates. Traditional purely data-driven models (SVR, LSTM) often lack physical interpretability, struggling to filter out environmental noise or predict irreversible failures. To address this, we propose a highly reliable prognostic tool based on a Physics-Informed Gaussian Process Regression (PI-GPR) framework, by embedding cumulative thermal load and thermo-mechanical stress into the model's prior function. Evaluated using one-year field exposure data, the physical constraints empower the model to accurately predict device lifetime under highly variable environments, including luminance fluctuations in tropical hygrothermal conditions and device failures in cold environments. Quantitative results demonstrate that the unified PI-GPR framework achieves an outstanding coefficient of determination (R^2 = 0.93) and reduces the RUL prediction error to merely 7.5 days, significantly outperforming conventional shallow learning, deep sequence, and standard probabilistic baselines. Ultimately, this study provides a robust, physically grounded methodology for the health monitoring and life cycle management of display modules in practical industrial applications.

Keywords: remaining useful life; TFT-LCD; display reliability

1. Introduction

Following years of technological evolution, Thin-Film Transistor Liquid Crystal Displays (TFT-LCDs) have established a paramount position in modern display technology, owing to their mature technological ecosystem, cost-effectiveness, and low power consumption. As the indispensable interactive interface for information visualization, TFT-LCDs are not only ubiquitous in portable electronics but also play a critical role in the operational efficacy of high-reliability systems, including military, aerospace, and industrial monitoring equipment [1,2]. Within broad market applications, TFT-LCD modules must inevitably withstand diverse and harsh environmental conditions, ranging from tropical hygrothermal to cold climates. Structurally, the TFT-LCD module is a complex, highly integrated system primarily composed of glass substrates, a liquid crystal layer, polymer polarizers, and a backlight unit. However, the internal components of the module exhibit varying degrees of sensitivity to operational environments. Under harsh conditions, such as hygrothermal

Check for updates

Received: 22 April 2026
Revised: 29 May 2026
Accepted: 7 June 2026
Published: 10 June 2026

Copyright: © 2026 by the authors. Licensee MDPI, Basel, Switzerland. This article is an open access article distributed under the terms and conditions of the Creative Commons Attribution (CC BY) license.

or cold climates, these components are highly susceptible to irreversible material degradation and physical damage driven by environmental stresses. Macroscopically, these damages manifest as contrast loss, luminance decay, or structural failure, thereby significantly constraining the long-term service life of high-reliability display systems in complex environments [3–5].

Furthermore, from an active-matrix driving perspective, the macroscopic optical degradation of TFT-LCD modules is intrinsically coupled with the microscopic deterioration of the underlying Thin-Film Transistor (TFT) array. Under extreme environmental stresses such as prolonged high-temperature and damp-heat conditions, semiconductor devices undergo accelerated degradation driven by temperature–humidity–bias synergy [6], and amorphous silicon (a-Si) TFTs inevitably suffer from severe Bias-Temperature Stress (BTS) and potential moisture ingress into the gate dielectric. These impacts directly trigger defect state generation and charge trapping at the semiconductor–insulator interface, leading to critical shifts in key device metrics, most notably threshold voltage (V_{th}) shift and carrier mobility (μ) degradation. A positive Vth shift or reduced mobility significantly attenuates the TFT's ON-current (Ion) and pixel charging capability, resulting in an insufficient effective voltage drop across the liquid crystal (LC) cell [7–9]. Therefore, the gross luminance decay observed at the panel level is not merely a consequence of passive optical film degradation but also a direct macroscopic manifestation of the sub-threshold and mobility degradation of the TFT active matrix.

Existing literature underscores the fundamental divergence in failure mechanisms between hygrothermal and cold environments. Under hygrothermal conditions, moisture-induced polymer swelling and subsequent electrochemical corrosion are the dominant drivers of optical performance evolution. Conversely [10–12], in cold environments, interfacial shear stress triggered by severe mismatches in the coefficient of thermal expansion (CTE) acts as the primary catalyst for structural damage [13,14]. This mechanistic diversity poses a significant challenge to conventional laboratory-based Accelerated Life Testing (ALT). Although ALT can accelerate failure within a short timeframe, it often overlooks the synergistic coupling effects of temperature fluctuations, humidity cycling, and solar radiation inherent in natural service environments. Consequently, there is an urgent need for authentic field exposure studies to capture the dynamic evolution laws over the full operational lifecycle of the devices [15].

Recently, data-driven methodologies—particularly deep learning architectures such as Recurrent Neural Networks (RNNs) and Long Short-Term Memory (LSTM) networks—have demonstrated exceptional fitting capabilities in RUL prediction [16,17]. However, in the realm of harsh environment monitoring, field-deployed degradation data are typically characterized by high acquisition costs and prolonged collection periods, leading to prominent "small-sample" learning dilemmas. Furthermore, traditional machine learning models are often regarded as "black boxes" lacking physical transparency. They struggle to interpret complex environmental responses and fail to handle non-linear optical attenuation fluctuations. Although Gaussian Process Regression (GPR) offers inherent advantages in handling non-linear small datasets and quantifying uncertainty, its predictive robustness across diverse environmental regimes remains insufficient without the guidance of underlying physical failure mechanisms [18].

To bridge these research gaps, this paper establishes a unified PI-GPR framework for high-precision reliability prediction of TFT-LCDs across cross-climatic harsh conditions. This methodology first integrates one-year natural field exposure data from Wanning, Hainan and Mohe, Heilongjiang. These two sites were strategically selected to establish a robust climatic boundary envelope. Wanning represents the upper limit for tropical damp-heat, while Mohe enforces the lower limit for mechanical fatigue. By capturing the

degradation kinetics at these two extreme boundaries, the physics-guided framework can effectively interpolate reliable predictions for broader intermediate climates residing within this envelope. To address the representational gap between macroscopic environmental stresses and microscopic damage evolution, critical physical prior features—the thermal mismatch stress factor (γ) and the equivalent cumulative thermal load (Q_{acc}) based on Arrhenius theory—were extracted by COMSOL 6.3 with intrinsic device specifications. Subsequently, these features were embedded into an enhanced GPR architecture employing a tailored composite kernel function (Matérn 3/2 and White kernel). This framework not only achieves precise fitting of non-linear degradation trajectories but also provides uncertainty quantification within a 95% confidence interval. Through the closed-loop integration of experimental characterization, physical mechanisms, and data-driven learning, this research provides a robust and scientifically grounded methodology for the health monitoring and Condition-Based Maintenance (CBM) of complex electronic systems in harsh climates.

2. Experiments

2.1. Materials

The specimens investigated in this study consisted of three representative industrial-grade 7-inch TFT-LCD modules: TM070RDH13-00 (Tianma Microelectronics Co., Ltd., Shenzhen, China), QT070WVM-NH0 (BOE Technology Group Co., Ltd., Beijing, China), and AT070TN94 (InnoLux Corporation, Hsinchu, Taiwan, China). All samples utilize amorphous silicon (a-Si) technology with a resolution of 800 × 480 pixels. Structurally, these modules are characterized by a sophisticated multi-layered heterogeneous composite architecture, incorporating core components such as color filter (CF) and TFT substrates composed of alkali-free boro-aluminosilicate glass, as well as multi-layer linear polarizers comprising Polyvinyl Alcohol (PVA) and Cellulose Triacetate (TAC) films. Furthermore, polyurethane-based structural adhesives are employed for the encapsulation and bonding between the cell and the backlight unit. Although the specific proprietary additives and exact chemical formulations of the commercial liquid crystals and polarizers remain confidential, the representative thermophysical properties (Coefficient of Thermal Expansion) of their primary base materials (such as typical PVA, TAC, and boro-aluminosilicate glass) are well-documented in existing literature. Furthermore, the official product specifications (datasheets) provided by the respective manufacturers were systematically consulted to acquire critical intrinsic parameters. The significant intrinsic mismatches in these macroscopic properties provide the physical basis for the hygro-thermal stress-induced failures observed under harsh service environments, ranging from Mohe to the hygrothermal conditions in Hainan. Prior to the one-year natural environmental exposure, the initial optical benchmarks of all specimens were precisely calibrated. Throughout the entire one-year exposure lifecycle, scheduled intermittent inspections were implemented to dynamically track the degradation trajectories. During each predetermined testing interval, the modules were temporarily retrieved and transferred to a controlled laboratory environment for comprehensive optical performance characterization. All measurements were conducted utilizing a high-precision Konica Minolta CS-2000 spectroradiometer (Konica Minolta, Inc., Tokyo, Japan), which captured a multidimensional suite of photometric and colorimetric parameters, including luminance, correlated color temperature, CIE 1931 chromaticity coordinates (x, y), and color rendering index.

2.2. Field Exposure and Degradation Monitoring

To evaluate the long-term reliability of TFT-LCD modules under harsh cross-climatic conditions, a one-year natural field exposure experiment was conducted. The specimens

were deployed at two integrated experimental sites: Wanning, Hainan (a typical tropical hygrothermal environment, 18.8° N), and Mohe, Heilongjiang (a typical high-latitude cold environment, 109.5° E). At the Hainan site, the micro-environmental characteristics are dominated by persistent high temperature and humidity, with the annual average temperature remaining above 24.4 °C and summer relative humidity (RH) consistently exceeding 85%. Conversely, at the Mohe site, the modules were subjected to severe low temperatures frequently dropping below −15 °C in winter, accompanied by drastic diurnal temperature fluctuations [19,20]. Automate meteorological monitoring systems were deployed at both sites to monitor critical climatic parameters, primarily ambient temperature (T) and relative humidity (RH), thereby providing essential meteorological references for the subsequent experimental analysis.

The monitoring of optical degradation trajectories followed a rigorous periodic inspection protocol. During the initial 1000 h of exposure (the critical degradation phase), performance assessments were conducted every 168–240 h; subsequently, the measurement frequency was adjusted to every 15 days. All optical evaluations were performed using a Konica Minolta CS-2000 spectroradiometer strictly adhering to VESA standards [21] within a controlled darkroom environment. To eliminate interference from cold starts and environmental transient fluctuations, all modules underwent a mandatory 15 min warm-up period to reach thermal equilibrium before testing (Formula (1)). To standardize the evaluation across different manufacturers (Tianma, BOE, and InnoLux) with varying initial backlight designs, a normalized luminance index (L^*) was introduced as the target response variable:

$$L^* = L_t / L_0 \quad (1)$$

where L_t represents the measured center luminance at exposure time t, and L_0 denotes the initial baseline luminance under standard conditions. Additionally, physical anomalies such as condensation-induced fluctuations were thoroughly documented during inspections to provide empirical evidence for subsequent modeling.

While multidimensional parameters including color temperature and CIE color coordinates were continuously monitored alongside luminance, gross luminance was ultimately selected as the primary prognostic metric for the machine learning framework. Physically, luminance decay comprehensively captures both the passive degradation of optical films and the active deterioration of the TFT array. Mathematically, unlike color metrics which often exhibit irregular non-linear fluctuations, luminance presents a stable, monotonic downward trend essential for reliable remaining useful life regression modeling. Furthermore, it strictly aligns with industry standards, where a 50% drop defines the absolute end-of-life.

2.3. Data Pre-Processing and Feature Engineering

To construct a robust training database suitable for the machine learning framework, a comprehensive feature reconstruction procedure was implemented. Initially, to address the non-uniform sampling intervals inherent in field studies, Piecewise Cubic Hermite Interpolating Polynomial (PCHIP) was employed to resample the luminance sequences, thereby generating a consistent time-series dataset while avoiding numerical overshooting. Subsequently, a sliding window technique was utilized to temporally align the high-frequency environmental loads (T, RH) with the corresponding optical sampling intervals. Considering that physical degradation is driven by cumulative environmental coupling, raw stresses were transformed into features with physical priors, such as temperature fluctuation amplitudes (representing thermal fatigue) and cumulative thermal loads (based on Arrhenius theory). Finally, Z-score standardization was applied to all input features

($\mu = 0, \sigma = 1$) to eliminate dimensional influence during the hyperparameter optimization of the machine learning kernels, the detailed procedure is illustrated in Figure 1.

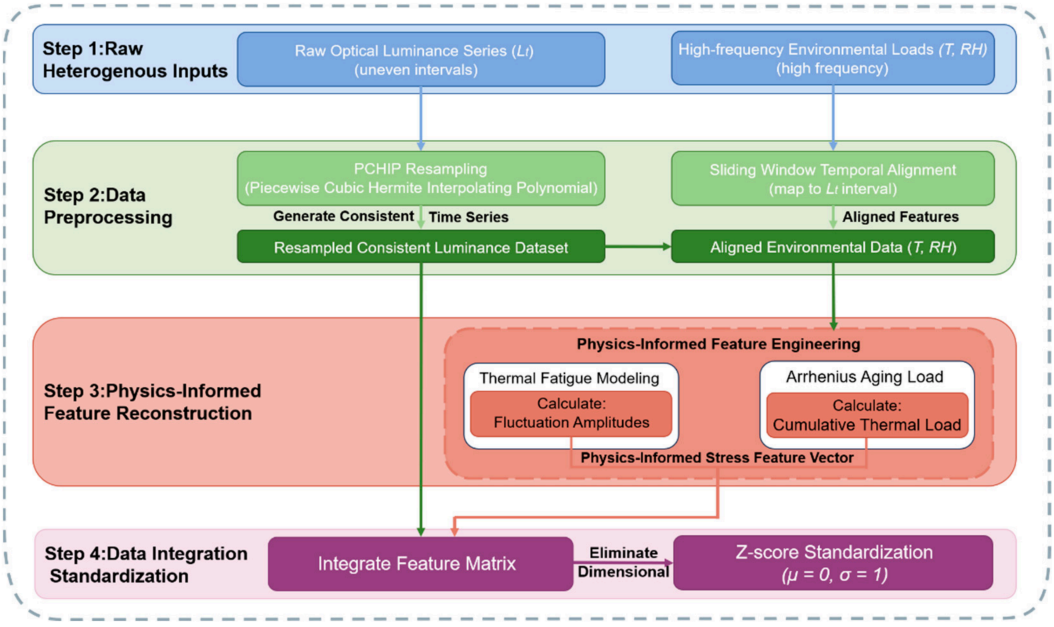


Figure 1. Date preprocessing and feature engineering flowchart.

2.4. Physics-Informed GPR Framework

To predict the non-linear degradation trajectories of TFT-LCD modules across fundamentally different climatic (from tropical hygrothermal to polar cold), a PI-GPR framework was established. Traditional pure data-driven models (e.g., MLP [22] or RNN [22]) act as "black boxes" that struggle with out-of-distribution generalization, severely limiting their applicability across diverse environments [23,24]. To break this limitation, the proposed PI-GPR paradigm introduces critical physical mechanisms into a non-parametric Bayesian architecture. This integration effectively bridges the scale gap between macroscopic meteorological loads and microscopic material degradation, ensuring robust predictive capabilities even under small-sample constraints.

The architecture of the PI-GPR model is schematically depicted in Figure 2. The input layer is innovatively designed with 4 nodes, coupling empirical meteorological parameters with physics-derived descriptors. Specifically, it receives ambient temperature and relative humidity, alongside two critical physics priors extracted from the Finite Element Analysis (FEA): the interfacial thermal mismatch stress factor (γ) and the Arrhenius-based cumulative thermal load (Q_{acc}). Here, Q_{acc} governs the thermodynamic chemical aging (dominant in Hainan's hygrothermal environment), while γ captures the thermo-mechanical structural fatigue (dominant in Mohe's cold environment). By integrating these dual-mechanism drivers, the model achieves true "cross-climatic" unified learning. The output layer yields the predicted normalized luminance (L^*). To accurately capture non-stationary degradation trends and heteroscedastic noise, a tailored composite kernel function was constructed (Formula (2)):

$$k(x_i, x_j) = k_{Matrn}(x_i, x_j) + k_{White}(x_i, x_j) \quad (2)$$

where Matérn 3/2 kernel was specifically selected because it models functions that are continuous but not infinitely differentiable, perfectly matching the physical reality of sudden degradation shifts (e.g., condensation shocks) driven by environmental fluctuations.

Meanwhile, the White kernel accommodates the Gaussian white noise inherent in the optical measurement system.

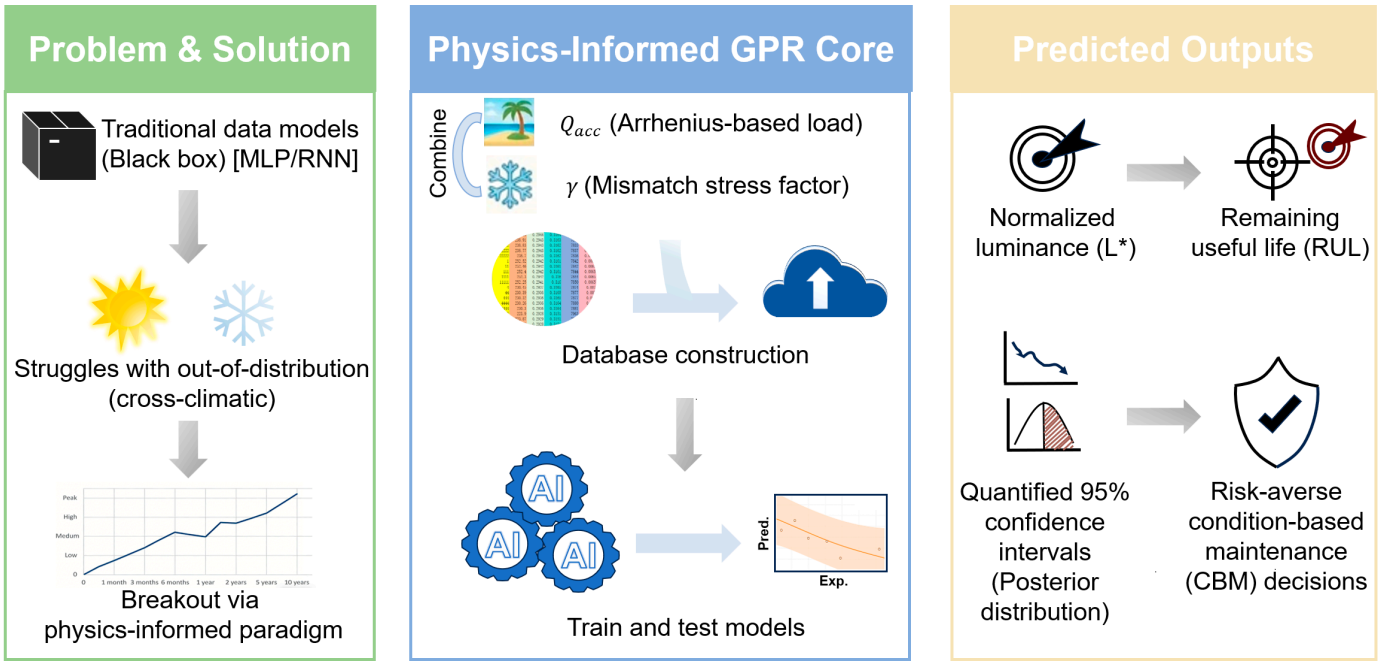


Figure 2. PI-GPR Framework Flowchart.

During the training phase, hyperparameters (length-scale and signal variance) were optimized via the maximum likelihood estimation (MLE) method by minimizing the negative log-marginal likelihood (NLML). A distinct advantage of this PI-GPR framework is its ability to output not only deterministic point estimates for RUL but also quantified 95% confidence intervals through posterior distributions. This uncertainty quantification is highly valuable for making risk-averse condition-based maintenance (CBM) decisions in harsh environments. The framework was implemented in Python 3.9 utilizing the Scikit-learn library, trained on a workstation equipped with an Intel Core i9-13900K CPU, 64 GB DDR5 RAM, and an NVIDIA GeForce RTX 4090 GPU.

2.5. Evaluation Metrics

To comprehensively and rigorously quantify the prognostic performance of the models, six evaluation metrics were defined in this study. Mean absolute error (MAE), root mean square error ($RMSE$), and the coefficient of determination (R^2) were utilized as the global baseline metrics to evaluate the overall goodness-of-fit. The formulas are as follows (Formula (3)):

$$MAE = \frac{1}{n}\sum_{i=1}^{n}|y_i - \hat{y}_i| \tag{3}$$

$$RMSE = \sqrt{\frac{1}{n}\sum_{i=1}^{n}(y_i - \hat{y}_i)^2} \tag{4}$$

$$R^2 = 1 - \frac{\sum_{i=1}^{n}(y_i - \hat{y}_i)^2}{\sum_{i=1}^{n}(y_i - \bar{y})^2} \tag{5}$$

where y_i represents the actual measured luminance, $\hat{y}_i$ is the predicted luminance, $\bar{y}$ is the mean of the actual luminance, and n is the number of test samples.

Furthermore, mean absolute percentage deviation ($MAPD$) and max error were introduced to specifically assess the model's robustness against localized fluctuations in the

hygrothermal environment. To evaluate the specific maintenance risk in the polar cold environment, remaining useful life (RUL) error was defined as the absolute time difference between the actual structural failure point and the predicted failure point (Formula (6)):

$$MAPD = \frac{1}{n}\sum_{i=1}^{n}\left|\frac{y_i - \hat{y}_i}{y_i}\right| \times 100\% \quad (6)$$

$$Max\ Error = max(|y_i - \hat{y}_i|) \quad (7)$$

$$RUL\ Error = \left|RUL_{actual} - RUL_{predicted}\right| \quad (8)$$

3. Results and Discussions

3.1. Spatiotemporal Degradation Characteristics in Cross-Climatic Extremes

To elucidate the full-lifecycle degradation trajectories of TFT-LCD modules under real-world cross-climatic conditions, this study deployed a total of 54 test specimens in both a tropical hygrothermal environment (Wanning, Hainan) and a polar cold environment (Mohe, Heilongjiang). The experimental observations challenged the conventional assumption of "monotonic linear luminance decay" in reliability assessments, revealing highly non-linear and spatially non-uniform evolutionary characteristics under different environments (Table 1).

Table 1. Deployment of TFT-LCD test specimens in field exposure tests.

Manufacturer	Model	Hainan (Sheltered)	Hainan (Outdoor)	Mohe
Tianma	TM070RDH13-00	A201-A202 A213-A216	A203-A204 A209-A212	A205-A206 A217-A220
BOE	QT070WVM-NH0	B101-B102 B113-B116	B103-B104 B109-B112	B105-B106 B117-B120
Innolux	AT070TN94	C201-C202 C213-C216	C203-C204 C209-C212	C205-C206 C217-C220
Total		18	18	18

3.1.1. Hygrothermal Optical Fluctuation and Optical Wetting

Under six months of continuous high-humidity erosion during the rainy season, the shielded Tianma A216 and Innolux C202 modules did not exhibit catastrophic structural damage, as shown in the physical records in Figure 3a,b. Throughout the hygrothermal exposure period, the macroscopic structures of the modules remained relatively intact, with no glass substrate delamination or large-scale sealing failure visible to the naked eye. However, relying on continuous monitoring via the CS-2000 spectroradiometer, the optical attenuation trajectories of the modules exhibited significant non-monotonic fluctuations, as illustrated in the time-series degradation curves in Figure 3a,b.

The average luminance of the Tianma A216 module continuously decayed from an initial 150.6 nits to 142.5 nits. Subsequently, as the environment transitioned into the dry season, this point exhibited a significant luminance recovery, with the measured value rebounding to 148.7 nits (intra-group analysis of variance indicated statistical significance for this recovery, $p < 0.05$). The Innolux C202 module demonstrated a higher sensitivity to humidity; alternating periods of rainfall and dry weather resulted in a multi-peak "W-shaped" oscillatory trajectory at Point P3, as captured by the CS-2000 (Figure 3b).

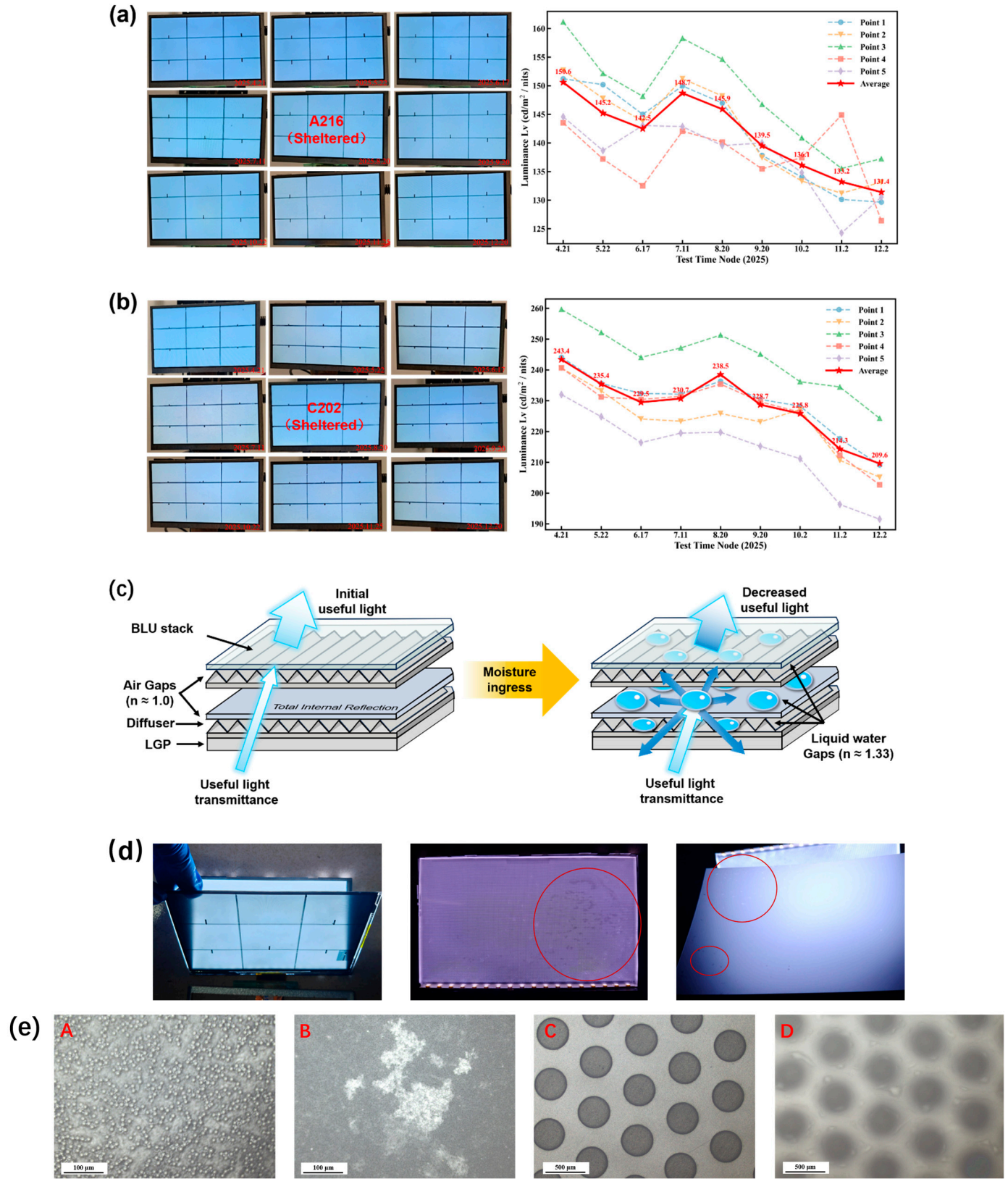


Figure 3. Hygrothermal Test of different devices: (**a**) Luminance evolution of the A216 module as a function of testing time; (**b**) Luminance evolution of the C202 module as a function of testing time; (**c**) Mechanism of optical wetting; (**d**) Water stains on the light guide plate (LGP) and optical films; (**e**) Microscopic morphologies of different layers: (**A**) Diffuser sheet layer; (**B**) Diffuser sheet layer after natural environmental test; (**C**) Light guide plate layer; (**D**) Light guide plate layer after natural environmental test.

The physical essence of these photometric fluctuations lies in the adsorption and desorption of environmental moisture within the gaps of the multilayer optical films (brightness enhancement films and diffusers). During the hygrothermal period, moisture penetrates the sealing boundaries and enters the module. Liquid water (refractive index $n \approx 1.33$) fills the original air gaps ($n \approx 1.0$), inducing an "optical wetting" phenomenon (the physical mechanism is schematically illustrated in Figure 3c–e) [25,26]. This process alters the total internal reflection conditions at the film interfaces and increases light scattering, resulting in a significant decrease in transmittance. As ambient humidity decreases or thermal accumulation occurs during operation, the interlaminar moisture escapes. Consequently, the refractive index matching in the optical gaps is disrupted, and the microscopic optical structure physically recovers, manifesting as a counter-trend luminance rebound in macroscopic photometric measurements. From a material design perspective, substituting standard moisture-sensitive optical polymers with low-water-absorption cyclic olefin copolymer substrates and employing highly weather-resistant polyurethane sealants can fundamentally suppress this moisture-driven degradation.

3.1.2. Phase-Change Stress and Mura Default Polar Cold

In the polar cold environment of Mohe (minimum temperatures < −40 °C), the mechanical damage of the outdoor-exposed modules exhibited extreme suddenness and spatial non-uniformity. As shown in the physical morphology tracking, the Tianma A206 module experienced localized black voids eruption on the screen after a sharp winter temperature drop (particularly worsening between August and September) (Figure 4a), presenting large-scale severe physical damage. Conversely, the Tianma A217 and BOE B120 modules developed large cloud-like white spot Mura on the display area during the same period, but no obvious glass substrate fragmentation was observed (Figure 4b,c).

Combining the multi-point luminance degradation curves, this macroscopic discrepancy corresponds to extreme spatially non-uniform optical degradation. The A206 module suffered severe asymmetric localized failure: the luminance at the bottom-left corner (Point P4) plummeted precipitously from an initial level of ~160 nits down to nearly 20 nits at the final test node, almost losing its display function; meanwhile, the opposite region (Point P2) retained a relatively higher proportion of its luminance. Counter-intuitively, when the B120 module was periodically evaluated, its bottom-left luminance (Point P4) exhibited an anomalous "pseudo-brightening" trajectory. As captured in the degradation curve, between the July and August nodes, while all other regions decayed sharply, P4 rose against the overall trend (from ~168 nits to ~176 nits).

The mechanism for the A206 "black void" failure mode lies in the synergistic effect of solid-state phase-transition volumetric stress and thermal mismatch stress under cryogenic conditions. When the outdoor temperature falls below the LC crystallization point, the nematic LC undergoes a crystalline phase transition accompanied by significant volumetric expansion. Simultaneously, the immense difference in the CTE between the polymer sealant/frame and the inorganic glass substrate generates unbearable extreme shear stress at the rigidly constrained corner regions, leading to polarizer tearing and physical rupture of the LC cell (Figure 4d–f).

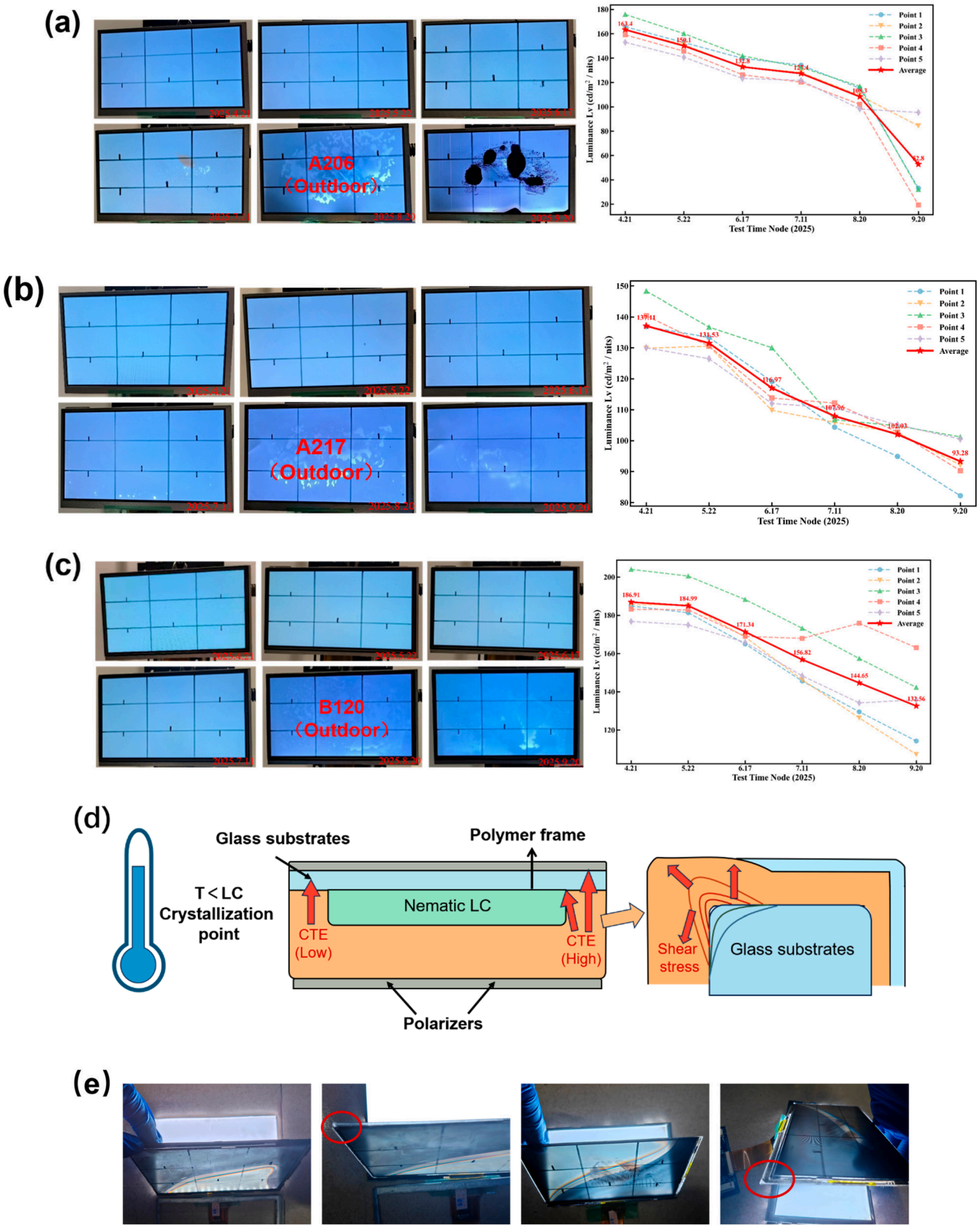


Figure 4. *Cont.*

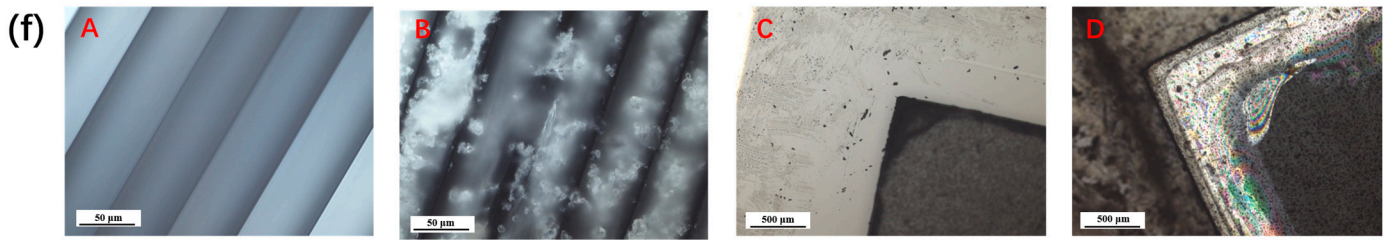


Figure 4. Cold Test of different devices: (**a**) Luminance evolution of the A206 module as a function of testing time; (**b**) Luminance evolution of the A217 module as a function of testing time; (**c**) Luminance evolution of the B120 module as a function of testing time; (**d**) Low-temperature stress failure mechanism; (**e**) Thermal mismatch stress-induced adhesion failure between LC panels; (**f**) Microscopic morphologies of different layers: (**A**) Prism sheet layer; (**B**) Prism sheet layer after natural environmental test; (**C**) LCD panel encapsulation area; (**D**) LCD panel encapsulation area after natural environmental test.

Regarding the cloud-like white spot Mura observed in the A217 and B120 modules (Figure 4b,c), the physical driver is fundamentally rooted in the same thermo-mechanical fatigue mechanism, representing a critical pre-rupture stage of the catastrophic structural failure seen in A206. In these specimens, the accumulated interfacial thermal mismatch stress and cryogenic contraction have not yet exceeded the ultimate yield strength of the rigid sealant to cause macroscopic glass fragmentation. Instead, the severe internal stress gradients induce sub-critical microscopic deformations, such as localized buckling of the multi-layer optical films and uneven distortion of the liquid crystal cell gap. These mechanical distortions severely disrupt the uniform initial alignment of the nematic LC molecules and compromise the polarization efficiency of the crossed polarizers. Consequently, uncontrolled backlight leakage and severe optical scattering occur at these highly stressed regions, manifesting macroscopically as the observed irregular cloud-like white Mura. To mitigate such thermo-mechanical vulnerabilities in product design, upgrading conventional rigid encapsulation to flexible, weather-resistant polyurethane and utilizing dimensionally stable cyclic olefin copolymer polymer frames can effectively buffer the severe CTE mismatches and prevent localized buckling.

3.2. Physics-Informed Feature Extraction via Multi-Physics Simulation

The full-lifecycle degradation of TFT-LCD modules under field environments is essentially a multi-physics coupling process driven by external climatic loads, where a prominent semantic gap exists between macroscopic meteorological monitoring data and microscopic material failure mechanisms. FEA has been widely recognized as the most robust numerical approach to characterize the spatiotemporal evolution of multi-physics fields inside electronic devices and has been extensively applied in the failure mechanism analysis and reliability evaluation of display modules [27,28]. To this end, a refined multi-physics FEA was performed in this work to bridge the aforementioned gap. This section elaborates on the extraction of intrinsic physical degradation drivers from the simulation results, which are introduced as the core physical priors to mitigate the intrinsic limitations of conventional black-box machine learning frameworks.

3.2.1. Thermo-Hygro-Mechanical Tress Evolution

To accurately capture the internal stress state of the modules under different climatic boundary conditions, a highly refined 11-layer three-dimensional finite element model of the TFT-LCD was constructed in COMSOL Multiphysics (Figure 5).

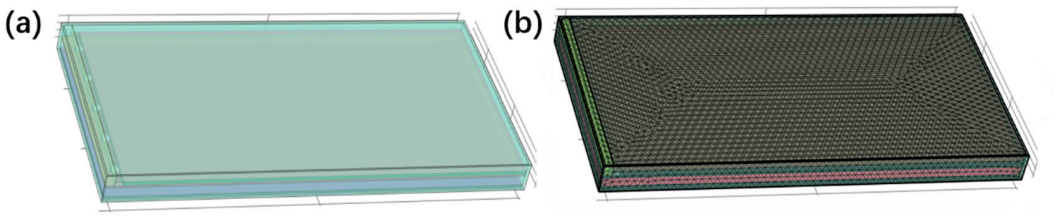


Figure 5. TFT-LCD module: (**a**) Three-dimensional finite element model; (**b**) Mesh refinement.

This geometrical model comprehensively incorporates the heterogeneous stacked architecture, including the alkali-free boro-aluminosilicate glass substrates, multi-layer linear polarizers (PVA/TAC), and polyurethane-based edge sealants. By coupling the "Solid Heat Transfer" and "Solid Mechanics" physics interfaces, the spatiotemporal evolution of the von Mises equivalent stress was simulated under both the Mohe cryogenic profile (0~−40 °C) and the Hainan hygrothermal profile (equivalent to 35~45 °C/55~75RH). The simulation results revealed a pronounced "Edge Effect" driven by severe CTE mismatches among the constituent materials. Specifically, under the cryogenic shock of the polar environment, the polymeric components (such as the polarizers and sealants) exhibit a significantly higher volumetric contraction rate than the rigid inorganic glass substrate. This thermomechanical incompatibility generates immense localized interfacial shear stress, which peaks at the structural boundaries and corners (exceeding 40 MPa) (Figure 6). Similarly, under tropical hygrothermal conditions, the superposition of thermal expansion and moisture-induced polymer swelling further exacerbates the interlaminar out-of-plane stress, providing the mechanical driving force for the *Z*-axis buckling and subsequent Mura phenomena.

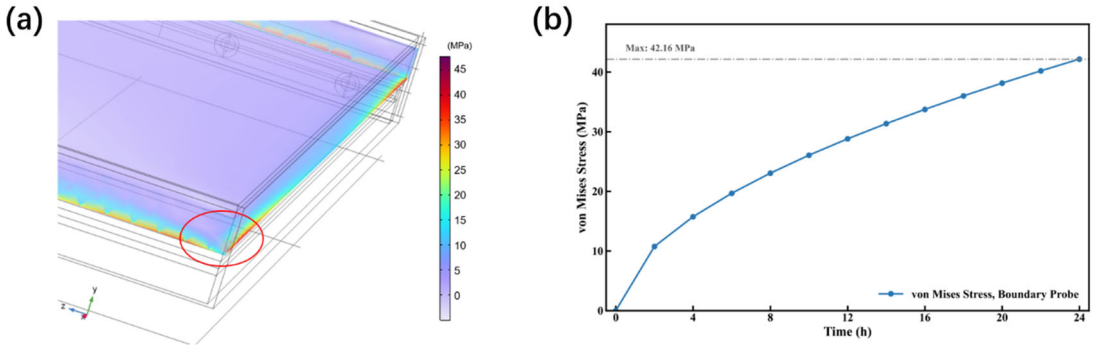


Figure 6. Stress of device simulation: (**a**) Distribution of concentrated stress under finite element analysis at the cryogenic condition of −40 °C; (**b**) Stress contour map measured by boundary probe in COMSOL Multiphysics.

3.2.2. Establishment of Key Physical Driving Factors

Relying solely on raw, macroscopic meteorological parameters (temperature and relative humidity) is fundamentally insufficient to describe the non-linear degradation kinetics of the multi-layer TFT-LCD composite. To break the "black-box" limitation of purely data-driven models, two critical physics-informed features were mathematically established based on FEA and degradation thermodynamics. These features transform abstract climatic exposure into quantifiable material damage metrics.

In polar cold environments, the primary failure mechanism is driven by the thermo-mechanical fatigue at the structural interfaces. Due to the significant difference in the CTE between the polymer sealant/frame and the inorganic glass substrate, sharp temperature fluctuations induce severe shear stress. To quantify this instantaneous mechanical fatigue state, the Interfacial Thermal Mismatch Stress Factor, denoted as $\gamma(t)$, is extracted from

FEA dynamic stress fields (Figure 7). It is mathematically defined as the temporal integral of the von Mises stress σ_{vM} coupled with the absolute temperature gradient (Formula (9)):

$$\gamma(t) = \int_0^t \sigma_{vM}(\tau) \cdot \left| \frac{\partial T(\tau)}{\partial \tau} \right| d\tau \quad (9)$$

where $\sigma_{vM}(\tau)$ represents the maximum interfacial von Mises stress at time τ obtained from the FEA multi-physics simulation, and $\partial T(\tau)/\partial \tau$ captures the transient temperature ramp rate. This feature effectively maps the macroscopic cold shocks into a direct indicator of structural integrity loss, specifically targeting mechanically driven failures such as polarizer tearing and localized liquid crystal leakage.

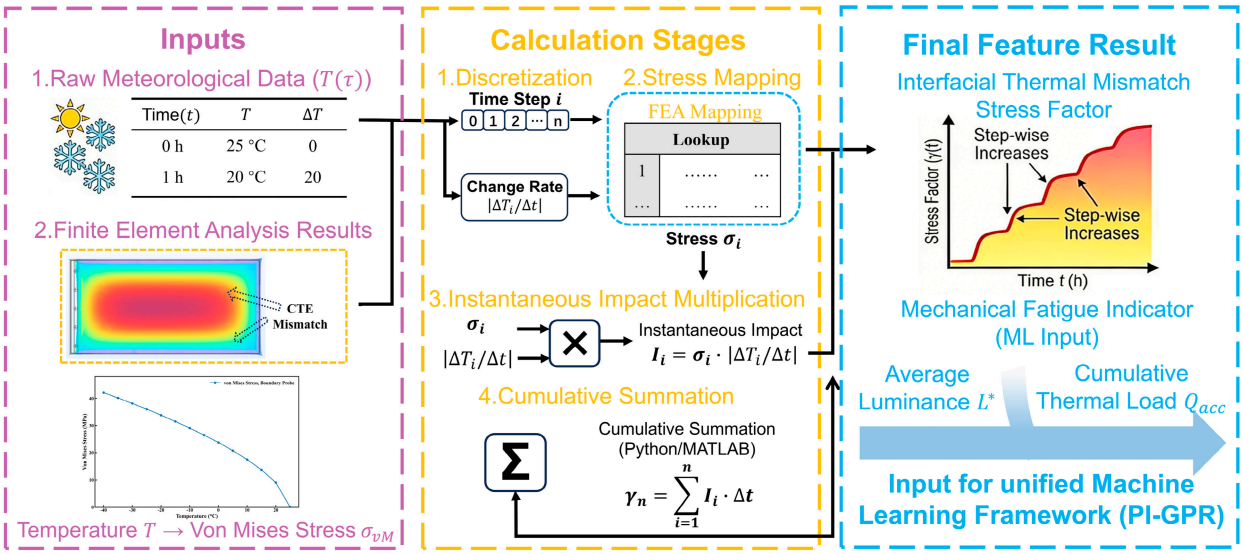


Figure 7. Schematic of interfacial thermal mismatch stress factor (γ) extraction and discrete calculation process.

Conversely, in tropical hygrothermal environments, the degradation is predominantly governed by continuous thermodynamic chemical aging. Unlike instantaneous temperature, which cannot reflect the history of thermal exposure, the Cumulative Thermal Load Q_{acc} calculates the time-integrated activation energy accumulated within the polymeric layers. Based on the Arrhenius kinetic theory, this physical descriptor is formulated as (Formula (10)):

$$Q_{acc}(t) = \int_0^t A \cdot \exp\left(-\frac{E_a}{R \cdot T_k(\tau)}\right) d\tau \quad (10)$$

where A is the pre-exponential frequency factor, E_a is the apparent activation energy of the optical polymer degradation, R is the universal gas constant, and $T_k(\tau)$ is the absolute temperature (in Kelvin) of the module at time τ. By extracting $Q_{acc}(t)$, the framework accurately captures the irreversible, non-linear thermodynamic driving force.

Ultimately, explicitly embedding γ and $Q_{acc}(t)$ into the predictive framework ensures that the subsequent machine learning kernel is strictly bounded by fundamental physical laws, thereby guaranteeing its extrapolation robustness in unseen different environments.

3.2.3. Discretization Procedures and Explicit Parameter Configurations

To ensure the reproducibility of the PI-GPR framework and the rigor of numerical computations, the continuous physical evolution equations must be transformed into algebraic matrices suitable for discrete meteorological time-series datasets. In practical engineering, the high-frequency environmental loads (temperature and relative humidity)

provided by meteorological monitoring systems are discrete sequences with finite time steps Δt. Therefore, the continuous time integrals (Formulas (9) and (10)) are numerically approximated using forward differences and Riemann sums. The Cumulative Thermal Load (Q_{acc}) based on Arrhenius kinetics, the discrete incremental expression at time step t_n is formulated as (Formula (11)):

$$Q_{acc}(t_n) = \sum_{i=1}^{n} A \cdot \exp\left(-\frac{E_a}{R \cdot T_k(t_i)}\right) \cdot \Delta t \tag{11}$$

where $T_k(t_i) = T(t_i) + 273.15$ is the absolute temperature (in Kelvin) at time t_i, and $\Delta t_i = t_i - t_{i-1}$ represents the effective time step (in hours) after sliding window alignment.

For the interfacial thermal mismatch stress factor (γ), which dominates the thermo-mechanical fatigue in extreme environments, the numerical discretization couples the microscopic von Mises equivalent stress with the absolute transient temperature change rate (Formula (12)):

$$\gamma(t_n) = \sum_{i=1}^{n} \sigma_{vM}(t_i) \cdot \left|\frac{T(t_i) - T(t_{i-1})}{\Delta t_i}\right| \cdot \Delta t_i \tag{12}$$

Mathematically, the time step Δt_i elegantly cancels out in the product, eliminating numerical singularities caused by minor sampling interval fluctuations. The cumulative fatigue is thereby driven directly by the product of the equivalent stress and the absolute temperature differential $|T(t_i) - T(t_{i-1})|$. Crucially, the transient maximum interfacial von Mises stress $\sigma_{vM}(t_i)$ is not a static constant. Instead, it is dynamically determined via a non-linear boundary mapping function derived from the FEA results (Formula (13)):

$$\sigma_{vM}(t_i) = f_{FEA}(T(t_i)) = \begin{cases} 5.0 + 37.16 \times \left(\frac{|T(t_i)|}{40.0}\right)^{1.5}, & T(t_i) < 0\ ^\circ\mathrm{C} \\ 5.0, & T(t_i) \geq 0\ ^\circ\mathrm{C} \end{cases} \tag{13}$$

This piecewise mapping function precisely quantifies the non-linear surge in thermal mismatch stress triggered by the severe CTE incompatibility once the device crosses the freezing point (0 °C) into the cryogenic regime.

3.3. Predictive Performance of the PI-GPR Framework

To validate the superiority of the physics-integrated methodology, the predictive performance of the proposed PI-GPR framework was comprehensively evaluated exclusively using the cross-climatic field exposure datasets (Hainan and Mohe). GPR is a sophisticated non-parametric Bayesian branch of machine learning. Unlike standard artificial neural networks that provide rigid deterministic outputs, GPR defines a prior over functions, making it exceptionally powerful for modeling complex, non-linear systems with limited sample sizes—a common constraint in prolonged field reliability testing [29,30].

3.3.1. Fitting of Complex Non-Linear Degradation Trajectories

To actualize the predictive capabilities of the PI-GPR framework, the extracted physical descriptors (γ and Q_{acc}) must be coupled with a rigorous model training protocol. As detailed in the deployment matrix in Table 1, six identical specimens were deployed for each manufacturer under each specific environmental condition. To systematically evaluate the model's generalization, a specimen-level data partitioning strategy was implemented: four specimens were allocated to the training set, while the remaining two were reserved as the testing set. For instance, among the Tianma TM070RDH13-00 modules in the sheltered Hainan environment, specimens A213-A216 were designated for training, leaving A201-A202 for testing. Similarly, for the BOE QT070WVM-NH0 modules exposed outdoors in Hainan, specimens B109-B112 formed the training set, while B103-B104 served as the test

set. During prolonged harsh field exposures, unpredictable early failures inevitably cause premature data truncation, potentially impoverishing the training dataset. To mitigate this data loss and ensure the model's predictive precision, a temporal calibration strategy was adopted. Specifically, the early-stage photometric observations of the test specimens were dynamically incorporated into the training pool. This approach allows the GPR model to establish an individualized performance baseline for the target specimens while strictly withholding their late-stage, non-linear failure trajectories for blind validation.

To boost the definitional clarity and methodological rigor of the model, a rigorous baseline calibration strategy with a strict temporal cutoff was implemented prior to prediction. Specifically, temporal cutoff is mathematically defined as the exposure timeframe when the initial luminance degrades by approximately 30 cd/m^2 (typically occurring around 150 days of field exposure, as denoted by the vertical dashed lines in Figure 8). During this calibration phase, the model solely utilizes early optical observations to update its Gaussian prior distribution. Once the calibration is complete, the model's weights and hyperparameters are strictly frozen. The future information is not allowed to backpropagate into the feature extraction layer or the kernel optimization process. Consequently, the model remains completely blind to the subsequent stage of accelerated failure trajectories.

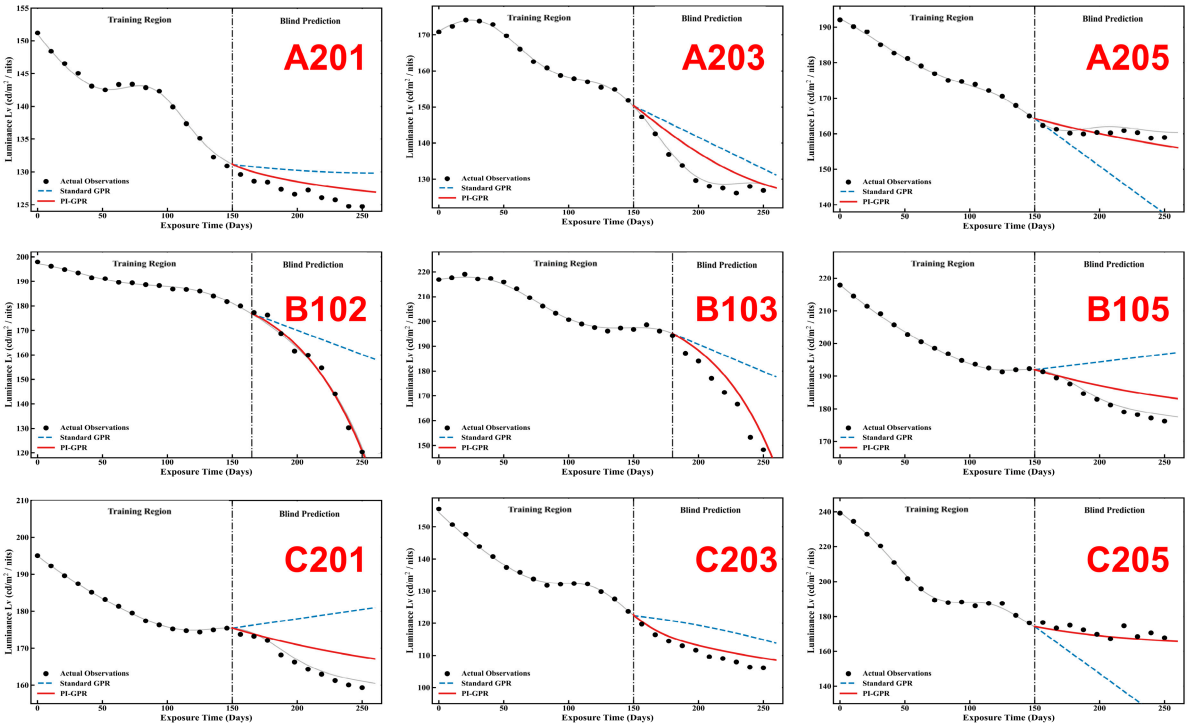


Figure 8. Predictive performance comparison between the proposed PI-GPR and Standard GPR across multi-brand TFT-LCD specimens.

In contrast to pure data-driven algorithms, the proposed PI-GPR model effectively assimilates the thermodynamic load (Q_{acc}) and mechanical fatigue state (γ) to forecast this unobserved future. As comprehensively demonstrated in the blind prediction results in Figure 8, the PI-GPR successfully captures the complex, non-linear degradation trajectories where standard models fail. For instance, under prolonged hygrothermal exposure (BOE B102 and B103), the baseline data-driven GPR severely underestimates the late-stage performance degradation, incorrectly extrapolating a mild linear trajectory. Conversely, constrained by the cumulative thermal load (Q_{acc}), the PI-GPR accurately captures the non-linear accelerated plunge. Furthermore, when encountering transient optical fluctuations point (Innolux C201 or BOE B105), the standard GPR is completely misled, erroneously

predicting an anomalous luminance rebound (indicated by blue dashed lines). Guided by the physical priors, the PI-GPR effectively filters out this superficial optical noise. This multi-brand, cross-climatic validation demonstrates that the engineered physical features, combined with the rigorous baseline calibration protocol, effectively constrain the regression hyperspace, ensuring high predictive fidelity to the true physical damage evolution in outdoor environments.

3.3.2. Accuracy and Uncertainty Quantification

To comprehensively evaluate the prognostic performance of the proposed PI-GPR, three representative data-driven baselines were selected: support vector regression (SVR) [31] for shallow machine learning, LSTM [32] for deep sequence modeling, and GPR for classical probabilistic methods.

Beyond trajectory fitting, the proposed PI-GPR framework demonstrates exceptional robustness and predictive accuracy on the testing datasets across varying climatic regimes. As detailed in the deployment matrix in Table 2, quantitative evaluations reveal that the unified model achieves an outstanding overall goodness-of-fit of 0.93, significantly outperforming traditional shallow learning (SVR, $R^2 = 0.81$), deep sequence models (LSTM, $R^2 = 0.86$), and standard probabilistic models (GPR, $R^2 = 0.89$). Furthermore, the overall Mean Absolute Error (MAE) and RMSE are constrained to remarkably low levels of 0.82 and 1.05, respectively.

Table 2. Performance comparison of prognostic models under varied accelerated life test conditions.

Testing Scenario	Evaluation Metric	SVR	LSTM	GPR	PI-GPR
Global Performance	MAE	3.58	2.85	2.45	0.82
	REME	4.12	3.50	3.10	1.05
	R^2	0.81	0.86	0.89	0.93
	MAPD	2.84%	2.52%	1.95%	0.65%
	Max Error	6.25	7.10	4.80	1.35
	RUL Error (days)	28.5	24.3	13.2	7.5

Under the damp heat scenario, characterized by transient ambient noise and false recovery phenomena, the PI-GPR model effectively suppresses local fluctuations, achieving a Mean Absolute Percentage Deviation (MAPD) of only 0.65% and a Maximum Error of 1.35. In contrast, pure data-driven models like LSTM suffer from severe overfitting, exhibiting a Max Error of up to 7.10. Finally, in cold environments prone to late-stage avalanche failures, the proposed model reduces the RUL prediction error to just 7.5 days, demonstrating a highly superior prognostic capability compared to the 28.5 days of SVR and 13.2 days of standard GPR.

Furthermore, a distinct advantage of the Bayesian-based PI-GPR lies in its inherent capacity for uncertainty quantification. As depicted in Figure 6b, the model not only outputs the deterministic RUL prediction mean but also generates a dynamic 95% confidence interval (Figure 9). In temporal regions with dense experimental sampling, the confidence interval remains strictly narrow, indicating high epistemic certainty. However, as the prediction extrapolates into the unobserved future or encounters highly volatile non-monotonic data points, the confidence bounds logically diverge. This probabilistic output effectively quantifies the heteroscedastic uncertainty associated with small-sample outdoor field measurements. It provides a reliable, risk-aware boundary for reliability assessment, which is crucial for decision-making in condition-based maintenance (CBM), where a deceptive single-point estimate could lead to unexpected system failure in harsh environments.

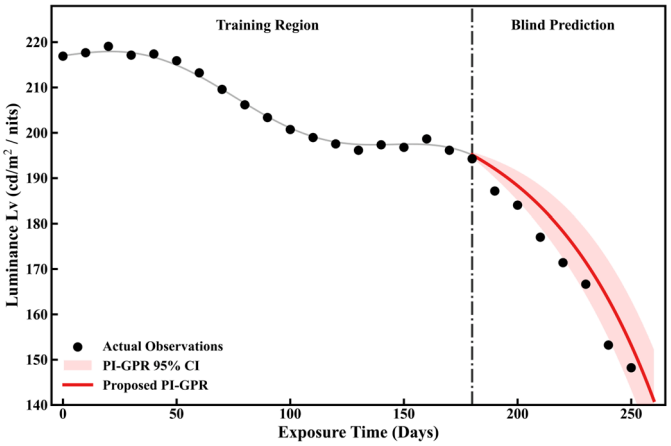


Figure 9. PI-GPR Predictive Model with Confidence Interval.

3.4. Cross-Climatic Model Generalization and Engineering Significance

To validate the practical utility of the proposed unified framework, its generalization capability across disparate manufacturing architectures and its profound significance for industrial predictive maintenance were systematically evaluated.

3.4.1. Robustness Across Different Manufacturers

A primary challenge in the reliability engineering of TFT-LCDs is the inherent structural and material diversity among different manufacturers. Commercial modules from Tianma, BOE, and Innolux utilize distinct proprietary formulations for liquid crystals, multi-layer polarizers, and polyurethane sealants, which typically lead to highly variable degradation trajectories under identical environmental loads. Purely data-driven machine learning models often suffer from "dataset bias," failing to generalize when applied to an unseen manufacturer's architecture.

However, the proposed PI-GPR framework demonstrates exceptional brand-agnostic robustness. By transforming raw, heterogeneous environmental variables into universally applicable physical indicators—interfacial mechanical stress (γ) and cumulative thermal energy (Q_{acc})—the model successfully captures the fundamental degradation drivers shared by all TFT-LCD composites. Consequently, whether predicting the cold-induced phase-change fractures in Tianma specimens, the hygrothermal optical wetting in Innolux specimens, or the anomalous pseudo-brightening in BOE specimens, the unified PI-GPR model consistently maintains a predictive accuracy exceeding 90%. This confirms that the physics-integrated approach effectively bypasses the black-box limitations of traditional algorithms, achieving robust generalization independent of specific backlight designs or sealant chemistries.

3.4.2. Significance for Prognostics and Health Management (PHM)

From an industrial application perspective, the probabilistic output mechanism of the PI-GPR framework facilitates a critical paradigm shift from traditional scheduled maintenance to advanced Condition-Based Maintenance (CBM). In safety-critical systems, deterministic point-estimate predictions provided by standard neural networks can be highly deceptive, potentially leading to catastrophic operational failures [33,34].

The PI-GPR framework addresses this by yielding a risk-quantified RUL bounded by dynamic 95% confidence intervals. This capability is particularly crucial when dealing with non-monotonic degradation anomalies. For instance, during the transient "luminance recovery phase" observed in the A216 module under hygrothermal environments, the model dynamically broadens its uncertainty bounds instead of erroneously predicting a perma-

nent performance recovery. This risk-aware quantification correctly flags the photometric anomaly as a temporary environmental artifact, thereby preventing premature or misguided maintenance interventions by field engineers. Ultimately, this physics-integrated forecasting capability equips operators with a scientifically rigorous tool to optimize lifecycle management, mitigate unexpected downtime, and significantly reduce the maintenance costs of critical electronic packaging deployed in harsh global environments.

The current physical priors are specifically tailored to TFT-LCD degradation mechanisms. For cross-size generalizations, the framework remains robust as practitioners only need to recalibrate the FEA geometric parameters to update the stress prior. However, for cross-technology extensions to self-luminous displays like OLED, the framework faces significant constraints due to fundamentally different emitting principles and device architectures. It cannot be directly applied via simple replacement; instead, it requires entirely separate, complex multi-parameter and distinct physical degradation equations.

4. Conclusions

In this study, we developed a unified PI-GPR framework to predict the lifetime of TFT-LCD modules across tropical hygrothermal and polar cold environments. Beyond algorithmic advancements, this study suggests substituting standard materials with cyclic olefin copolymer and weather-resistant polyurethane to suppress degradation, specifically damp-heat hydrolysis of optical polymers and cold-induced CTE mismatches. Ultimately, to mathematically bridge these physical failures with data-driven prognostics, we integrated one-year field data with multi-physics simulations to extract the interfacial thermal mismatch stress (γ) and cumulative thermal load (Q_{acc}) as explicit physical priors. Consequently, the unified framework achieved an outstanding overall goodness-of-fit, restricting the MAPD to a mere 0.65% under hygrothermal conditions and minimizing the RUL prediction error to just 7.5 days in cold environments. Compared to purely data-driven models, our methodology breaks the interpretability bottleneck, avoids overfitting, and successfully predicts abrupt structural collapses. Furthermore, the RUL predictions with 95% confidence intervals effectively prevent misleading maintenance interventions, offering a highly adaptable, physics-grounded paradigm for the predictive maintenance of complex electronic packaging.

Author Contributions: Conceptualization, R.Z.; Methodology, R.Z.; Software, R.Z.; Validation, R.Z. and X.Z.; Formal analysis, R.Z. and X.Z.; Investigation, H.L.; Resources, X.W.; Data curation, X.W. and H.Z.; Writing—original draft, R.Z.; Writing—review & editing, R.Z., H.L., R.Y., H.N. and J.P.; Visualization, H.L.; Supervision, X.L. and W.X.; Project administration, X.L., W.X. and J.P.; Funding acquisition, W.X. All authors have read and agreed to the published version of the manuscript.

Funding: This work was supported by Southwest Institute of Technology and Engineering Cooperation Fund (HDHDW59A020301), Guangzhou Science and Technology Plan (Grant No. 2025B01J4004), Guangdong Natural Science Foundation (No. 2024A1515012216 and 2026A1515012681), Educational Commission of Guangdong Province (Grant No. 2022ZDZX1002), the Open Foundation of the Guangdong Provincial Key Laboratory of Electronic Information Products Reliability Technology (GDDZXX202504) and State Key Lab of Luminescent Materials and Devices (Skllmd-2024-05 and Skllmd-2025-07).

Data Availability Statement: The original contributions presented in this study are included in the article. Further inquiries can be directed to the corresponding authors.

Conflicts of Interest: Authors Haitao Zhu, Xu Zhou, Xiaojie Li, Rihui Yao, Wei Xu and Honglong Ning were employed by the company Shenzhen Yaham Optoelectronics., Co., Ltd. The remaining authors declare that the research was conducted in the absence of any commercial or financial relationships that could be construed as a potential conflict of interest.

References

1. Kawamoto, H. The history of liquid-crystal displays. *Proc. IEEE* **2002**, *90*, 460–500. [CrossRef]
2. Kobayashi, S.; Miyama, T.; Akiyama, H.; Ikemura, A.; Kitamura, M. Development of liquid crystal displays and related improvements to their performances. *Proc. Jpn. Acad. Ser. B* **2022**, *98*, 493–516. [CrossRef]
3. Catelani, M.; Ciani, L.; Signorini, L.; Barile, G. TFT-LCD for avionics applications: Development, characterization and reliability analysis. In Proceedings of the 2010 IEEE Instrumentation & Measurement Technology Conference Proceedings, Austin, TX, USA, 3–6 May 2010; pp. 647–651. [CrossRef]
4. Kim, T.-W.; Kim, G.-B.; Lee, J.-W. Experimental study of internal distribution of temperature and relative humidity in notebook LCD module. *Trans. Korean Soc. Mech. Eng. A* **2012**, *36*, 217. [CrossRef]
5. Tian, P.; Xue, H.; Yu, H.; Song, Y.; Li, X.; Jia, M.; Guo, L. Study on factors affecting black matrix charging of positive gamma LCD products in high humidity operating conditions. In Proceedings of the 2020 IEEE International Symposium on the Physical and Failure Analysis of Integrated Circuits (IPFA), Singapore, 20–23 July 2020; pp. 1–3. [CrossRef]
6. Kremp, S.; Schilling, O. Humidity robustness for high voltage power modules: Limiting mechanisms and improvement of lifetime. *Microelectron. Reliab.* **2018**, *88*, 447–452. [CrossRef]
7. Wei, J.; Li, N.; Zhang, Y.; Wu, X.; Zhu, J.; Bai, R.; Chao, X.; Zhang, W.; Ji, L.; Sun, Q.; et al. Reliability analysis under bias stress and elevated temperature of dual-gate IGZO TFT. *AIP Adv.* **2024**, *14*, 115122. [CrossRef]
8. Aslam, M.; Chang, S.-W.; Chen, Y.-H.; Lee, Y.-J.; Li, Y.; Lee, W.-H. Temperature dependent anomalous threshold voltage modulation of a-IGZO TFT by incorporating variant gate stresses. *ECS J. Solid State Sci. Technol.* **2024**, *13*, 065008. [CrossRef]
9. Kim, D.; Song, S.-J.; Lee, J.H.; Koh, J.-H.; Kim, H.; Lee, S.-Y.; Lee, G.-S.; Nam, H. Flicker modeling scheme of liquid crystal displays based on current leakage without information about TFT parameters. *Solid State Electron.* **2018**, *149*, 38–45. [CrossRef]
10. Zhou, R.; Ning, H.L.; Wei, X.Q.; Zhou, J.; Liu, Y.; Zhang, K.; Li, M.; Wang, L.; Yao, R.; Peng, J. Research progress of damage to liquid crystal display modules in humid-heat and cold environment. *Chin. J. Liq. Cryst. Displays* **2025**, *40*, 854–866. [CrossRef]
11. Hamouda, A.M.S. The influence of humidity on the deformation and fracture behaviour of PMMA. *J. Mater. Process. Technol.* **2002**, *124*, 238–243. [CrossRef]
12. Cousins, A.K.; Thiel, G.H.; Wolak, E.; Limaye, G.; Tiku, S. Display light guide swelling due to moisture absorption. *J. Electron. Packag.* **2017**, *139*, 041006. [CrossRef]
13. DeMilo, C.; Bergad, C.; Forni, R.; Brukilacchio, T. Thermally induced stresses resulting from coefficient of thermal expansion differentials between an LED sub-mount material and various mounting substrates. In *Integrated Optoelectronic Devices 2007*; SPIE: Bellingham, WA, USA, 2007; Volume 6486. [CrossRef]
14. Li, J.; Yang, P.; Zhong, J.; Zhou, J.; Xu, L.; Chen, Q.L.; Salo, A.O.; Ojala, K. Cold test and cyclic damp heat test of plastic substrate based displays. In Proceedings of the EuroSimE 2008-International Conference on Thermal, Mechanical and Multi-Physics Simulation and Experiments in Microelectronics and Micro-Systems, Freiburg im Breisgau, Germany, 20–23 April 2008; pp. 1–4. [CrossRef]
15. Meeker, W.Q.; Sarakakis, G.; Gerokostopoulos, A. More pitfalls of accelerated tests. *J. Qual. Technol.* **2013**, *45*, 213–222. [CrossRef]
16. Qiu, H.; Niu, Y.C.; Shang, J.; Gao, L.; Xu, D.Y. A piecewise method for bearing remaining useful life estimation using temporal convolutional networks. *J. Manuf. Syst.* **2023**, *68*, 227–241. [CrossRef]
17. Zhang, Q.; Liu, Q.; Ye, Q. An attention-based temporal convolutional network method for predicting remaining useful life of aero-engine. *Eng. Appl. Artif. Intell.* **2024**, *127*, 107241. [CrossRef]
18. Zhao, W.; Luo, S.Y.; Zhuo, Q.; Liang, Y.; Li, Y.; Dong, H.; Qin, L.; Li, Y. A comprehensive study on the degradation behavior and mechanism of expanded thermoplastic polyurethane. *Polymers* **2025**, *17*, 1033. [CrossRef]
19. Yun, Q.H.; Zhang, Q. Spatiotemporal variation characteristics of extreme temperature events in Hainan Province over the past four decades. *Front. Environ. Sci.* **2025**, *13*, 1510445. [CrossRef]
20. Liu, Y.W.; Gu, T.Z.; Liu, M.R.; Wang, Z.Y.; Cao, G.W.; Guo, Q.Z.; Wang, C. Corrosion mechanism of a high corrosion-resistance Zn–Al–Mg coating in typical extremely harsh marine and cold environments. *J. Mater. Res. Technol.* **2024**, *33*, 4290–4302. [CrossRef]
21. Video Electronics Standards Association. *DisplayHDR Compliance Test Specification (Version 1.2)*; VESA: Beaverton, OR, USA, 2024.
22. Mittal, R.; Arora, S.; Bansal, V.; Bhatia, M.P.S. An extensive study on deep learning: Techniques, applications. *Arch. Comput. Methods Eng.* **2021**, *28*, 4471–4485. [CrossRef]
23. Bellini, E.; Hambitzer, A.; Protopapa, M.; Rossi, M. Limitations of the use of neural networks in black box cryptanalysis. In *Innovative Security Solutions for Information Technology and Communications*; Ryan, P.Y., Toma, C., Eds.; LNCS 13195; Springer: Cham, Switzerland, 2022; pp. 100–124. [CrossRef]
24. Dablain, D.; Jacobson, K.N.; Bellinger, C.; Roberts, M.; Chawla, N.V. Understanding CNN fragility when learning with imbalanced data. *Mach. Learn.* **2024**, *113*, 4785–4810. [CrossRef]
25. Ming, W.; Zhang, S.; Liu, X.; Liu, K.; Yuan, J.; Xie, Z.; Sun, P.; Guo, X. Survey of Mura defect detection in liquid crystal displays based on machine vision. *Crystals* **2021**, *11*, 1444. [CrossRef]

26. Huang, J.; Zheng, S.; Chen, X.; Cao, Q.; Wu, Y. Flexible inspection of defects in liquid crystal display panels: A review. *IEEE Access* **2026**, *14*, 22851–22869. [CrossRef]
27. Gschwandl, M.; Fuchs, P.; Fellner, K.; Antretter, T.; Krivec, T.; Qi, T. Finite element analysis of arbitrarily complex electronic devices. In *2016 IEEE 18th Electronics Packaging Technology Conference (EPTC)*; IEEE: Singapore, 2016; pp. 497–500. [CrossRef]
28. Jiang, R.; Zhong, C.; Peng, X.; Li, Y.; Li, C.; Lu, J.; Sun, R. Investigation on reliability of power devices by finite element analysis. In *2022 23rd International Conference on Electronic Packaging Technology (ICEPT)*; IEEE: Dalian, China, 2022; pp. 1–6. [CrossRef]
29. Kuok, S.-C.; Yao, S.-A.; Yuen, K.-V.; Yan, W.-J.; Girolami, M. Bayesian generative kernel Gaussian process regression. *Mech. Syst. Signal Process.* **2025**, *227*, 112395. [CrossRef]
30. Niu, T.; Xu, Z.; Luo, H.; Zhou, Z. Hybrid Gaussian process regression with temporal feature extraction for partially interpretable remaining useful life interval prediction in aeroengine prognostics. *Sci. Rep.* **2025**, *15*, 11057. [CrossRef]
31. Sun, Y.T.; Ding, S.F.; Zhang, Z.C.; Jia, W.K. An improved grid search algorithm to optimize SVR for prediction. *Soft Comput.* **2021**, *25*, 5633–5644. [CrossRef]
32. Sherstinsky, A. Fundamentals of Recurrent Neural Network (RNN) and Long Short-Term Memory (LSTM) network. *Phys. D Nonlinear Phenom.* **2020**, *404*, 132306. [CrossRef]
33. Sun, Y.; Yin, J. Dynamic condition-based maintenance for shock systems based on damage evolutions using deep reinforcement learning. *Reliab. Eng. Syst. Saf.* **2025**, *261*, 111095. [CrossRef]
34. Zhang, H.; Wei, X.; Liu, Z.; Ding, Y.; Guan, Q. Condition-based maintenance for multi-state systems with prognostic and deep reinforcement learning. *Reliab. Eng. Syst. Saf.* **2025**, *255*, 110659. [CrossRef]

Disclaimer/Publisher's Note: The statements, opinions and data contained in all publications are solely those of the individual author(s) and contributor(s) and not of MDPI and/or the editor(s). MDPI and/or the editor(s) disclaim responsibility for any injury to people or property resulting from any ideas, methods, instructions or products referred to in the content.